

Title: Dendrites endow artificial neural networks with accurate, robust and parameter-efficient learning

Authors: Spyridon Chavlis¹, Panayiota Poirazi^{1,*}

Affiliations:¹Institute of Molecular Biology and Biotechnology, Foundation for Research and Technology-Hellas, Heraklion, Crete 70013, Greece; *corresponding author: poirazi@imbb.forth.gr

Abstract

Artificial neural networks (ANNs) are at the core of most Deep learning (DL) algorithms that successfully tackle complex problems like image recognition, autonomous driving, and natural language processing. However, unlike biological brains who tackle similar problems in a very efficient manner, DL algorithms require a large number of trainable parameters, making them energy-intensive and prone to overfitting. Here, we show that a new ANN architecture that incorporates the structured connectivity and restricted sampling properties of biological dendrites counteracts these limitations. We find that dendritic ANNs are more robust to overfitting and outperform traditional ANNs on several image classification tasks while using significantly fewer trainable parameters. This is achieved through the adoption of a different learning strategy, whereby most of the nodes respond to several classes, unlike classical ANNs that strive for class-specificity. These findings suggest that the incorporation of dendrites can make learning in ANNs precise, resilient, and parameter-efficient and shed new light on how biological features can impact the learning strategies of ANNs.

Introduction

The biological brain is remarkable in its ability to quickly and accurately process, store, and retrieve vast amounts of information while using minimal energy¹. Artificial Intelligence (AI) systems, on the other hand, are notoriously energy hungry²⁻⁴ and often fail on tasks where biological systems excel, such as continual and transfer learning⁵⁻⁷. The most widely used AI method is deep learning (DL)⁸, which is applied in areas like computer vision⁹ and natural language processing¹⁰ and can even achieve superhuman performance in very specific tasks^{11,12}. However, the number of trainable parameters needed to achieve such performance is large leading to generalization failures due to overfitting¹³, as well as energy consumption levels that are not sustainable¹⁴. Moreover, unlike the brain, DL methods still fail to achieve high-performance accuracy under noisy settings^{15,16} and tasks where information changes in a continuous manner¹⁷. This dichotomy between biological and artificial intelligence systems suggests that drawing inspiration from the brain may help enhance the efficiency of DL models, bringing them one step closer to emulating the biological way of information processing.

DL architectures rely heavily on multilayered artificial neural networks (ANNs) inspired by their biological counterparts. In these networks, artificial nodes are typically constructed as linearly weighted sums of their inputs followed by a nonlinearity, roughly imitating how the soma or axon of biological neurons integrates inputs¹⁸, and learning occurs via changes in the connection strengths (weights) between these nodes¹⁹. In contrast, biological neurons are much more complex, consisting of a soma, an axon, and numerous dendrites that enable them to process thousands of synaptic inputs in parallel, in ways that differ extensively

between cell types²⁰. Although the somatic and axonal functionalities of biological neurons are well captured in artificial neurons, the dendritic computations are currently missing.

Biological dendrites, because of their ability to generate local regenerative events (dendritic spikes)^{21,22}, share a similar spiking profile as the neuronal soma. As a result, biological neurons can act as multi-layer ANNs²³⁻²⁶, able to perform complex computations^{27,28}, such as logical operations^{29,30}, signal amplification and segregation^{31,32}, coincidence detection³³⁻³⁶, multiplexing³⁷ and filtering of irrelevant or noisy stimuli^{38,39}. Consequently, dendrites are thought to underlie complex brain functions, including perception^{40,41}, motor behavior^{42,43}, fear learning⁴⁴⁻⁴⁶, and memory linking⁴⁷. Moreover, dendrites can help achieve such functions in an efficient manner. For example, they enable learning with few plastic synapses⁴⁸, forming memories using small neuronal populations²⁴, and increasing storage capacity^{49,50}. Given the high computational power of dendrites and the associated benefits in biological networks^{27,51}, the current design of artificial neurons seems outdated. Incorporation of dendritic properties would likely empower ANNs⁵²⁻⁵⁴, fostering more effective, efficient, and resilient learning behaviors like those seen in biological networks.

The above proposition is supported by recent studies that have integrated dendritic structures and their properties into traditional ANNs⁵⁵⁻⁵⁸, showing promising results on machine learning (ML) tasks⁵⁹⁻⁶⁴. For instance, adding active dendrites in ANNs was shown to enhance the network's ability to learn continually⁶³, while including a specific dendritic nonlinearity improved performance in a multitask learning scenario⁶⁵. However, to achieve improved performance, these studies have either sacrificed biological plausibility⁶⁴, used a very large number of trainable parameters⁶³, or were applied to very simple tasks⁵⁸.

Here, we propose a bio-realistic dendritic architecture that aims to improve learning in ANNs trained with the backpropagation algorithm. In the proposed architecture, inputs are fed into the dendritic layer, which is, in turn, connected to the somatic layer in a sparse and highly structured manner (**Figure 1**). Moreover, input sampling is inspired by the receptive fields of neurons in the visual cortex^{66,67} and amounts to sampling a restricted part of the input as opposed to the entire image, which is typically done in ANNs. By incorporating dendritic structural and sampling features, the new dendritic ANN models match or outperform traditional ANNs on several image classification tasks while using orders of magnitude fewer trainable parameters. These improvements are due to better utilization of trainable weights and a different learning strategy used by dendritic versus traditional ANNs, which also helps counteract overfitting. Overall, our findings suggest that dendrites can augment the computational efficiency of ANNs without sacrificing their performance accuracy, opening new avenues for developing bio-inspired ML systems that inherit some of the major advantages of biological brains.

Results

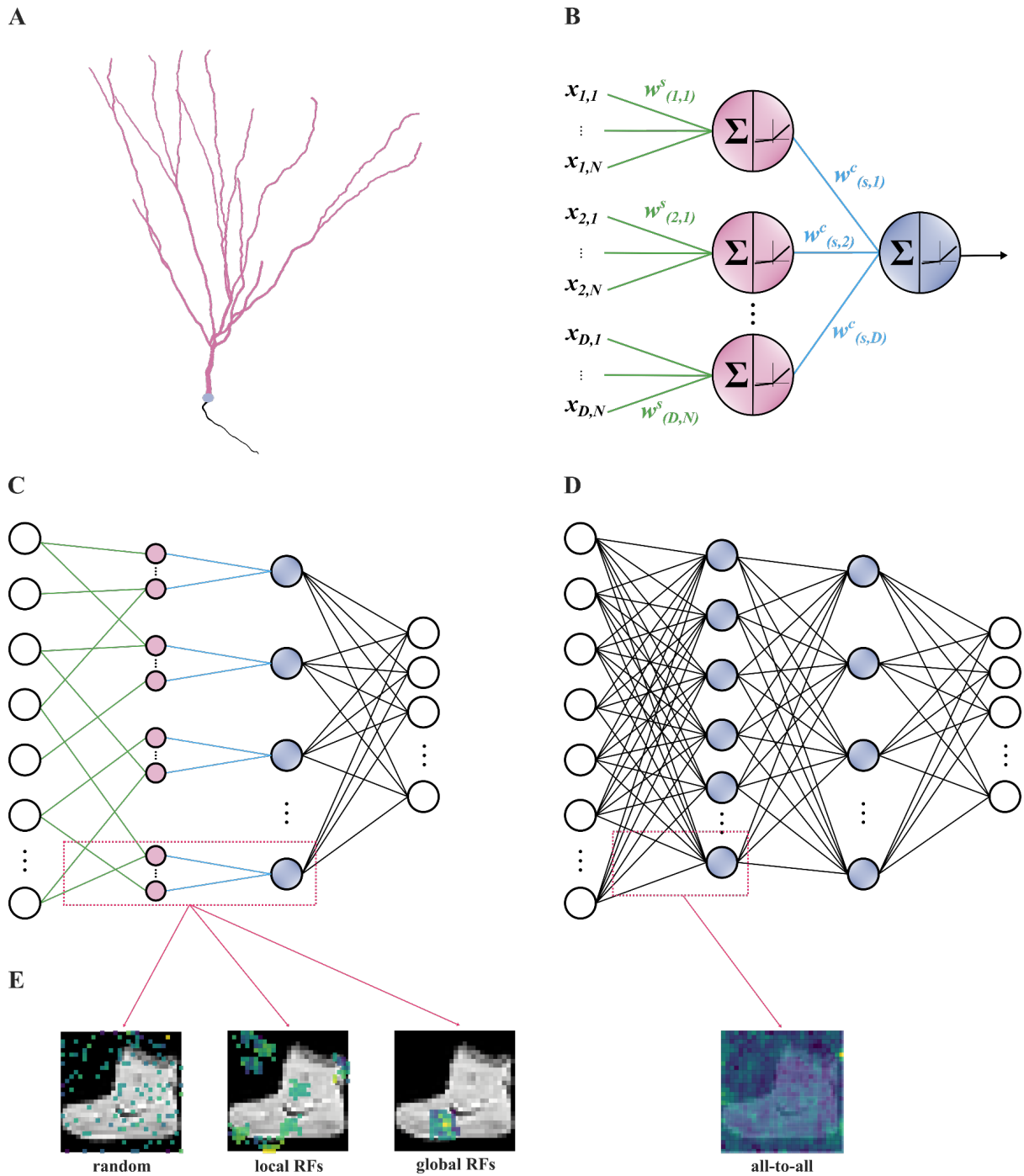


Figure 1. Schematic representation of the dendritic ANN (dANN). **A.** Example of a hippocampal granule cell based on which we constructed the artificial dendritic neuron in **B** (neuromorpho.org⁶⁸). **B.** The proposed neuron model consists of a somatic node (blue) connected to several dendritic nodes (pink). All nodes have a nonlinear activation function. Each dendrite is connected to the soma with a (cable) weight, $W_{(d,s)}^c$, where d and s denote the dendrite and soma indices, respectively. Inputs are connected to dendrites with (synaptic)

weights, $\mathbf{W}_{(d,n)}^s$, where d and n are indices of the dendrites and input nodes, respectively. $d \in \{1, D\}, n \in \{1, N\}$, N denotes the number of synapses each dendrite receives, and D the number of dendrites per soma s . **C.** The dendritic ANN architecture. The input is fed to the dendritic layer (pink nodes), passes a nonlinearity, and then reaches the soma (blue nodes), passing through another nonlinearity. Dendrites are connected solely to a single soma, creating a sparsely connected network. **D.** Typical fully connected ANN with two hidden layers. Nodes are point neurons (blue) consisting only of a soma. **E.** Illustration of the different strategies used to sample the input space: random sampling of input features (dANN-R), local receptive fields (dANN-LRF) and global receptive fields (dANN-GRF). The vANN samples the input space in an all-to-all manner. Examples correspond to the synaptic weights of all dendrites connected to the first somatic unit. The colormap denotes the magnitude of each weight.

To explore the role of dendrites in efficient learning, we developed a dendritic ANN (dANN) model with structured connectivity that loosely mimics the morphology of biological neurons (**Figure 1A**). In this model, each dendrite acts as a typical point neuron: it linearly sums its weighted inputs (synapses) and passes the sum through a nonlinearity. The dendritic activations are subsequently multiplied by the cable weights and summed at the soma before going through a second nonlinearity (**Figure 1B**). To train the model using ML platforms (e.g., TensorFlow, PyTorch), we implemented it as a traditional ANN with two sparsely connected hidden layers, representing the dendritic and somatic units, respectively, and a fully connected output layer (**Figure 1C**). For comparison purposes, we also implemented a fully connected, vanilla ANN (vANN) with the same number of layers (**Figure 1D**). Moreover, we developed three types of dANN models whereby we sampled the input space in different ways: a) random sampling of input features (dANN-R), b) local receptive fields (dANN-LRF) where each dendrite samples from a spatially restricted part of the image and c) global receptive fields (dANN-GRF) where all dendrites belonging to a soma sample from

the same spatially restricted part of the image. On the other hand, the vANN, as a fully connected architecture, samples the input space in an all-to-all manner (**Figure 1E**). We then tested the learning capabilities of our models on various image classification tasks (**Figure S2**) using the same hyperparameters, optimization algorithm, and loss function (see *Methods*). To ensure fair comparisons, we tested equivalent network architectures for all models, i.e., consisting of the same number of nodes in each hidden layer (**Figure S1**).

Dendritic ANNs are more accurate, robust, and efficient than vanilla ANNs on image classification.

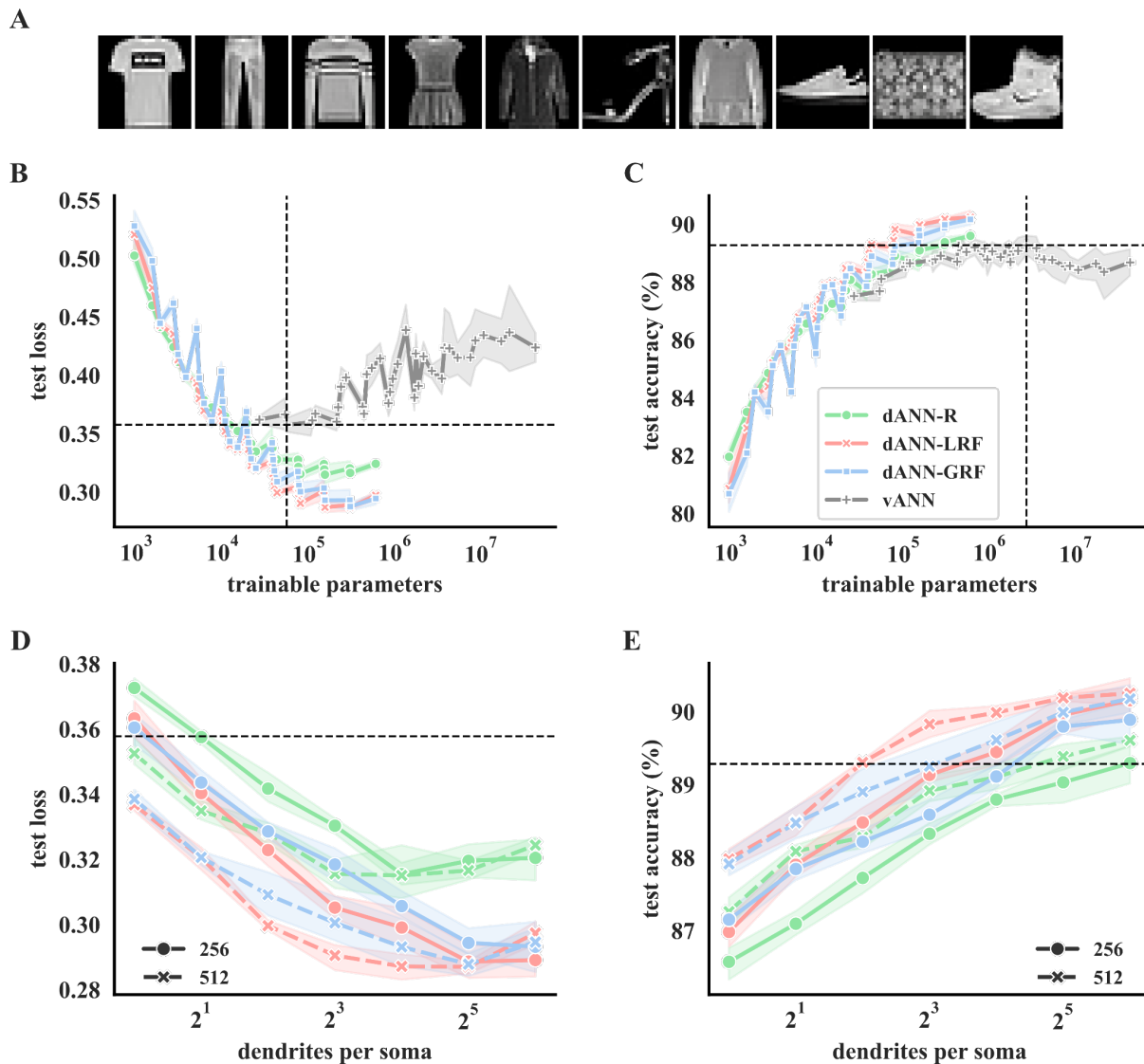


Figure 2. Dendritic features improve learning on Fashion MNIST classification. **A.** The Fashion MNIST dataset consists of 28×28 grayscale images of 10 categories. **B.** Average test loss as a function of the trainable parameters of the four models used: A dendritic ANN (dANN) with random inputs (green), a dANN with LRFs (red), a dANN with GRFs (blue), and the vANN (grey). Horizontal and vertical dashed lines denote the minimum test loss of the vANN and its trainable parameters, respectively. The x -axis is shown in a logarithmic scale (\log_{10}). **C.** Similar to **B**, but depicting the test accuracy instead of the loss. **D.** Test loss as a function of the number of dendrites

per somatic node for the three dANN models. The linestyle (solid and dashed) represents different somatic numbers. The dashed horizontal line represents the minimum test loss of the vANN (512-256 size of its hidden layers, respectively). The x -axis is shown in a logarithmic scale (\log_2). **E.** Similar to **D**, but showing the test accuracy instead of the loss. The dashed horizontal line represents the maximum test accuracy of the vANN (2048-512 size of its hidden layers, respectively). For all panels, shades represent three standard deviations across $N=5$ initializations for each model.

We first tested the learning capabilities of all models against the Fashion MNIST (FMNIST) dataset (**Figure 2A**). We found that dANNs achieve better learning and combat overfitting much more effectively than vANN models for both size-matched and larger vANN architectures (in terms of trainable parameters). This is evidenced by a consistently lower test loss (**Figure 2B**) for all dANN models compared to vANNs of the same number of trainable parameters. Importantly, the vANN models exhibit overfitting as the model size increases (**Figure 2B**), while this does not occur for dANNs, suggesting that dendrites may serve as regularizers⁶⁹. Moreover, the best performance of the vANN is achieved by dANNs with much fewer trainable parameters (**Figure 2C**), suggesting that dendrites render ANNs more efficient. Among the three dANN configurations, the local receptive field dANN (dANN-LRFs) is the most efficient, as it reaches maximum accuracy and minimum loss with one order of magnitude fewer trainable parameters than the vANN. In addition, we found that, as expected, learning improves with network size (lower loss: **Figure 2D**, better accuracy: **Figure 2E**) and that the type of input sampling is very important. Specifically, the use of random, local, or global receptive fields offset overfitting and improve accuracy across all dANN models compared to the vANN that uses all-to-all sampling. These findings

suggest that dendritic features, implemented here as structured connectivity and restricted input sampling, improve the performance accuracy of dANNs, as well as their efficiency and resilience to overfitting.

To substantiate our results on dendritic features, we tested the dANN models on five additional benchmark datasets (**Figure 3, Table 1**). As with FMNIST, we found that the best dANN models consistently outperformed the best vANN in terms of both accuracy and loss (**Table 1** and **Supplementary Table 1**). Moreover, similarly to FMNIST, we found that dANNs are much more efficient than vANN for all datasets. Specifically, they can match the accuracy (**Figure 3A**) and loss (**Figure 3B**) of the best vANN using 1-3 orders of magnitude fewer trainable parameters. It is worth noting that for more difficult tasks, like the CIFAR10 dataset, the difference in efficiency between dANNs and vANNs is more prominent.

To quantify this efficiency difference, we formulated the efficiency score metrics, which normalize the best accuracy (**Figure 3C**) and the corresponding loss (**Figure 3D**) that a given model can achieve with the number of trainable parameters used (see *Methods*). We found that all dANNs consistently exhibit higher efficiency than vANNs. Overall, these experiments confirm that dendritic features can greatly improve the performance accuracy and efficiency of classical ANNs across numerous image classification tasks.

Table 1. Top test accuracy scores obtained by each model on five benchmark datasets across various configurations and their corresponding test loss. Performance accuracy and loss are listed as mean \pm standard deviation over $N=5$ initializations for each model.

	MODEL PERFORMANCE – TOP ACCURACY				
Models	MNIST	FMNIST	KMINST	EMNIST	CIFAR10
	Test accuracy (%)				
dANN-R	98.090 \pm 0.0583	89.612 \pm 0.0870	91.076 \pm 0.0811	82.745 \pm 0.2568	52.458 \pm 0.4347
dANN-LRF	98.466 \pm 0.1058	90.256\pm0.2237	91.928\pm0.0643	83.166 \pm 0.0893	56.966 \pm 0.9796
dANN-GRF	98.576\pm0.0809	90.182 \pm 0.2164	90.046 \pm 0.2915	83.779\pm0.2064	56.998\pm0.4875
vANN (8e6)	98.034 \pm 0.2742	89.288 \pm 0.3654	91.552 \pm 0.6629	83.381 \pm 0.2681	49.082 \pm 1.2092
	Test loss				
dANN-R	0.0644 \pm 0.0013	0.3245 \pm 0.0028	0.5068 \pm 0.0045	1.0591 \pm 0.0225	1.4612 \pm 0.0172
dANN-LRF	0.0483 \pm 0.0018	0.2975 \pm 0.0042	0.4374\pm0.0037	0.6105 \pm 0.0048	1.2684\pm0.0230
dANN-GRF	0.0471\pm0.0022	0.2947\pm0.0052	0.5757 \pm 0.0335	0.5605\pm0.0077	1.3398 \pm 0.0217
vANN	0.0967 \pm 0.0116	0.4040 \pm 0.0066	0.8246 \pm 0.0791	2.0860 \pm 0.0476	2.0455 \pm 0.1375

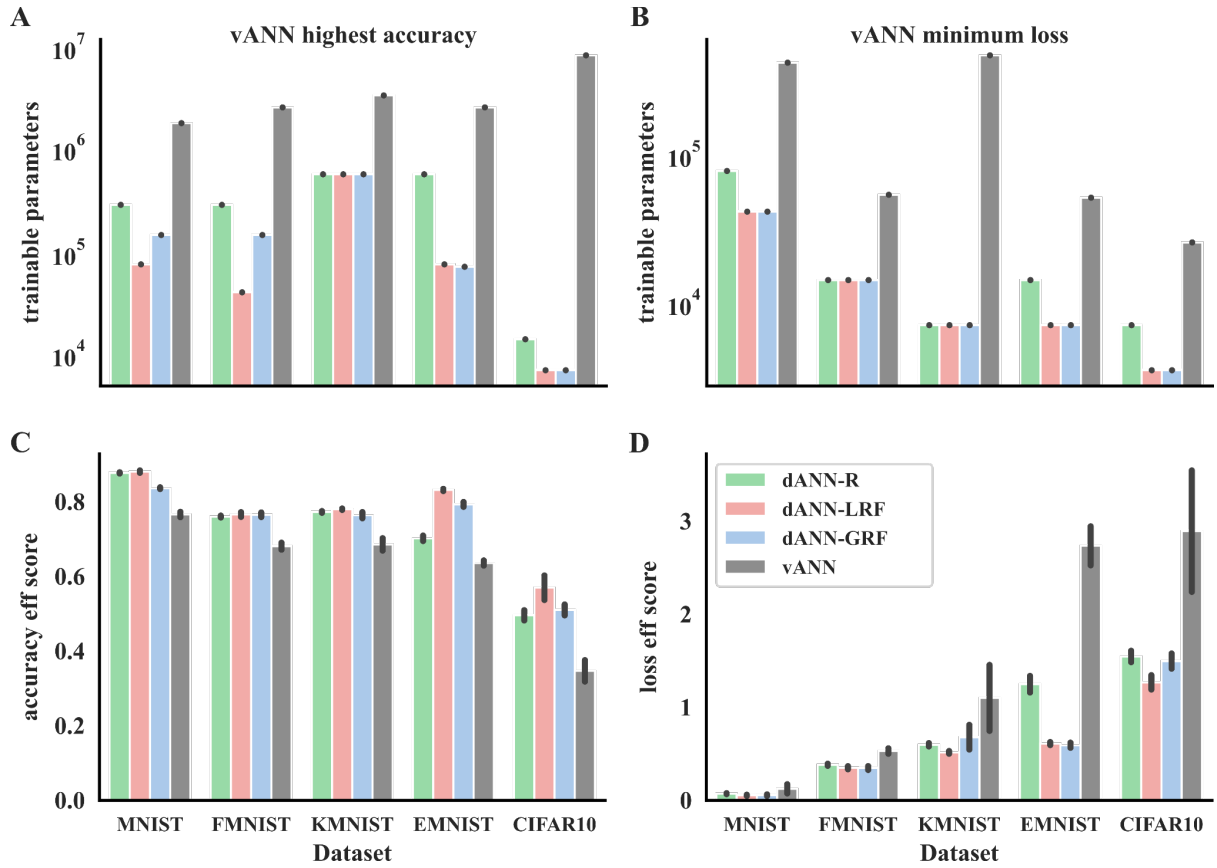


Figure 3. Dendrites improve performance across various benchmark datasets. **A.** Number of trainable parameters that each model needs, dANN (green), dANN-LRF (red), and dANN-GRF (blue), to match the highest test accuracy of the respective vANN (grey). **B.** The same as in B, but showing the number of trainable parameters required to match the minimum test loss of the vANN (grey). **C.** Accuracy efficiency score for all models and all datasets tested. Test accuracy is normalized with the logarithm of trainable parameters. The score is bounded in $[0, 1]$. **D.** Same as in C, but showing the loss efficiency score. Again, we normalized the test score with the logarithm of the trainable parameters. The score is bounded in $[0, \infty)$. In all barplots the errorbars represent three standard deviations across $N=5$ initializations for each model.

dANNs employ a distinct learning strategy and achieve better resource utilization

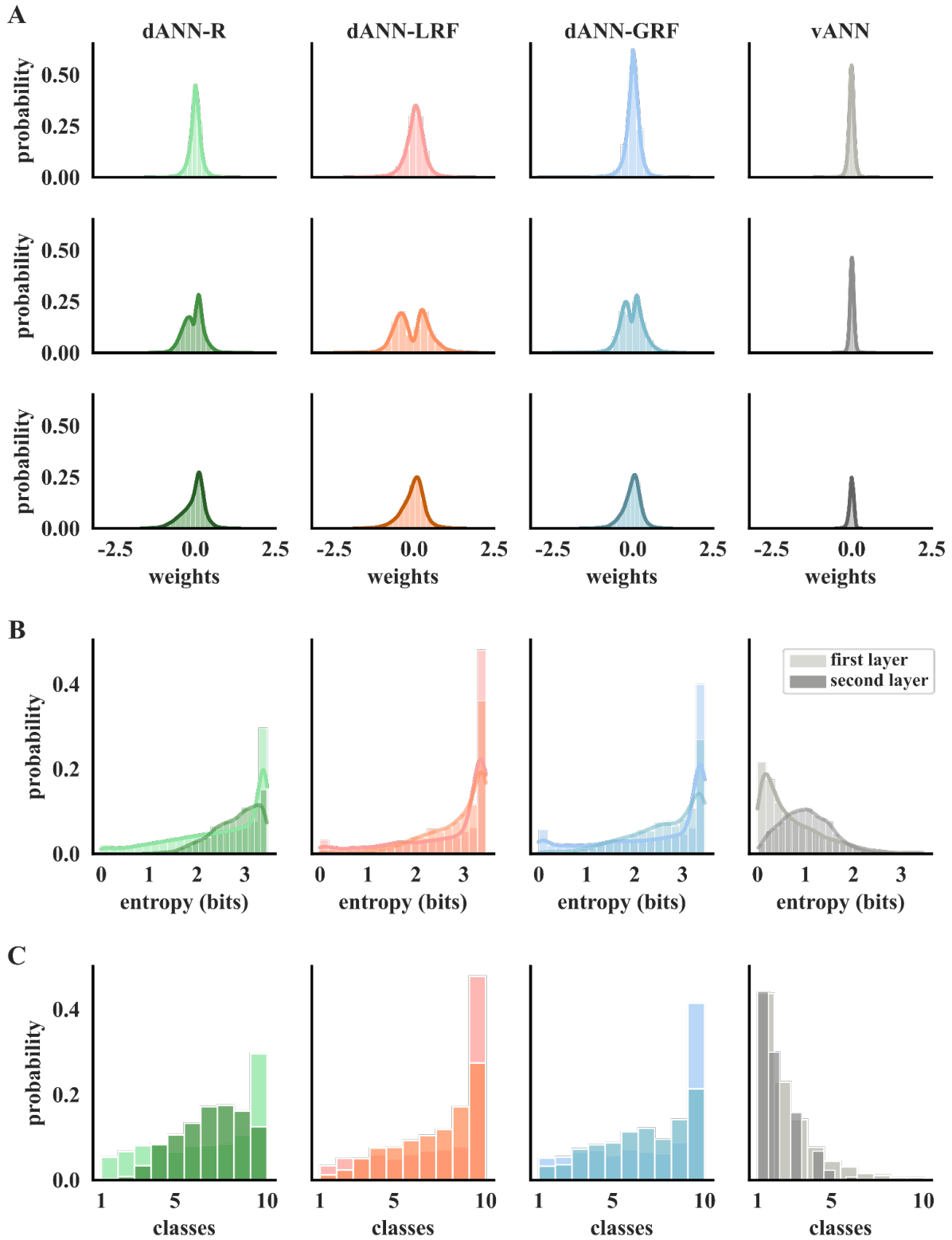


Figure 4. dANN models improve resource utilization and solve the task using a different learning strategy. **A.** Weight probability density functions after training for dANN-R, dANN-GRF, dANN-LRF, and vANN. The density functions are built by concatenating all weights across $N=5$ initializations for each model. First hidden layer (top row), second hidden layer (middle row), and output layer (bottom row) weights are shown. Both x and y axes are shared across all subplots for visual comparison among the density plots. **Supplementary Table 2** contains the kurtosis, skewness, and range of all KDE plots. **B.** Probability density function of the entropy (bits) for the first (normal color) and second (shaded color) hidden layer, respectively. Entropies are calculated using the activations of each layer for all test images of FMNIST (see *Methods*). Silent nodes have been excluded from the visualization. Higher values signify mixed selectivity, whereas low values indicate class specificity. **C.** Probability density functions of selectivity for both layers (different color shades) and all models (columns). For all histograms, the bins are equal to the number of classes, i.e., for the FMNIST dataset.

To better understand why dANN models outperform vANNs, we analyzed their weight distributions post-learning. We found a broader distribution, i.e., larger range of values, of synaptic (layer 1) weights for dANNs compared to vANN (**Supplementary Table 2** and **Figure 4A**, top row) and a bimodal distribution of dANN cable (layer 2) weights, all centered around zero (**Supplementary Table 2** and **Figure 4A**, middle row). For the dANN-LRF model, in particular, there were very few cable weights close to zero, indicating that the model effectively utilizes all trainable parameters of this layer. In contrast, in the vANN model, weights follow a Gaussian-like distribution centered around zero, suggesting that many weights are not as effectively utilized. Finally, the distribution of the output layer weights in dANNs is broader than in the vANN model (**Supplementary Table 2** and

Figure 4A, bottom row). These observations suggest that dANNs make better use of their trainable parameters, especially their cable (second layer or dendrosomatic) weights, compared to the second hidden layer of the vANN.

To delineate how the nodes of the different models contribute to a decision, we looked into their selectivity. First, we calculated the information entropy, which measures how class-specific a node is. High entropy values indicate mixed selectivity, whereby the node is active for more than one class, while low values indicate class specificity. We found opposite entropy distributions between dANNs and the vANN. This means that dANN models primarily have mixed-selective nodes in both hidden layers, while vANNs primarily have class-specific nodes. This difference was even more pronounced for dANNs with global or local RFs (**Figure 4B**).

To assess whether the observed differences in entropy map onto node specificity, we formulated the selectivity index, which counts how many classes a given node responds to. Specifically, if a node is active (activation greater than zero for a given image) for more than 400 images of a specific class, corresponding roughly to 40% of testing images, its selectivity index for that class is set to one. As with entropy distributions, we found that in dANNs, both layers consist primarily of mixed-selective nodes, while the vANN contains primarily class-specific nodes (**Figure 4C**). These observations suggest that dANN and vANN models employ different strategies to solve the same classification task.

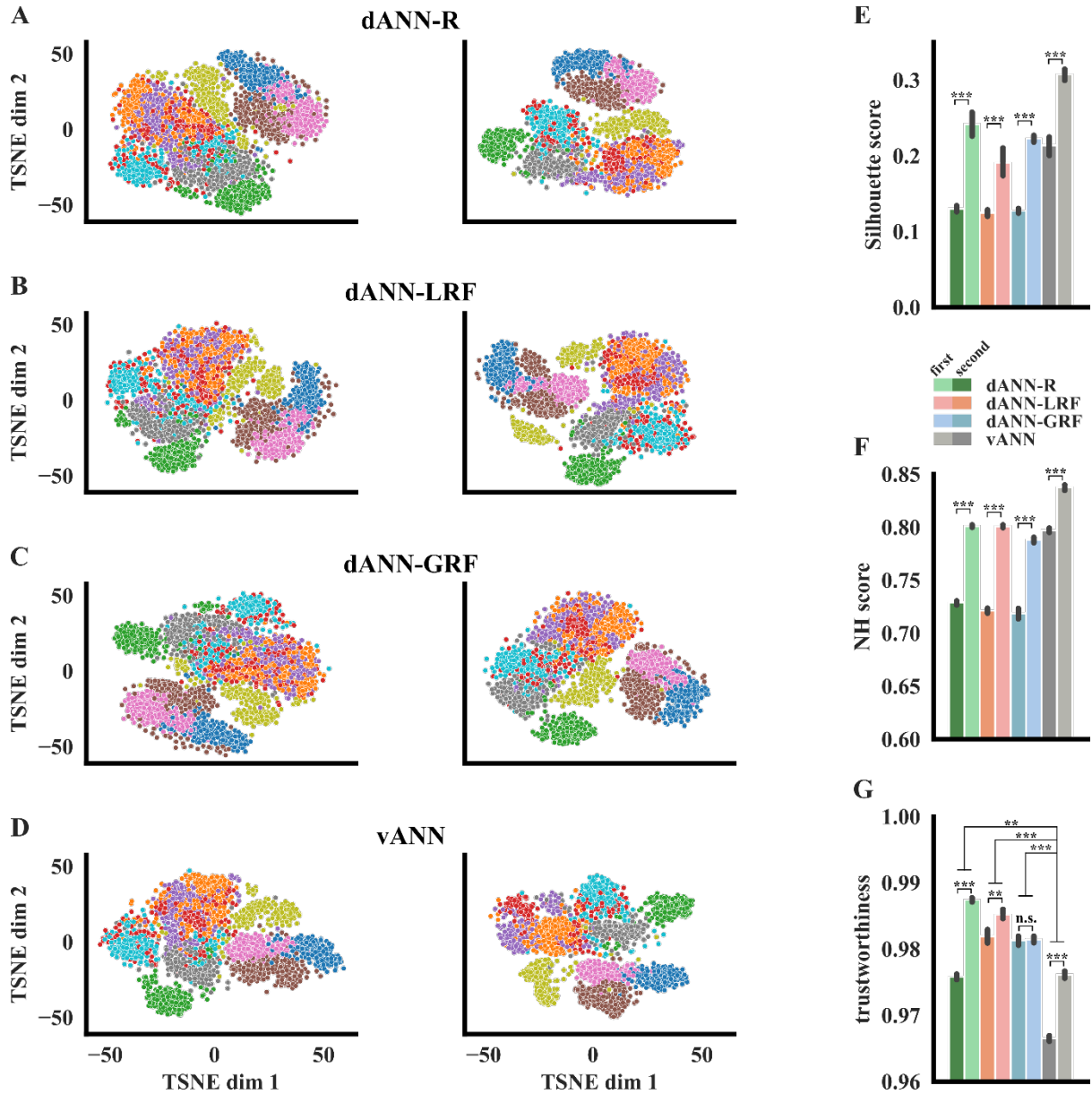


Figure 5. Learned representations. **A-D.** TSNE projections of the activations for the first (left column) and the second (right column) hidden layers corresponding to the three dANN and the vANN models. Different colors denote the image categories of the FMNIST dataset. **E.** Silhouette scores of the representations (2-way ANOVA: model $F(3,32)=112.68$, $p<10^{-3}$, layer $F(1,32)=459.70$, $p<10^{-3}$, model x layer $F(3,32)=4.87$, $p<10^{-2}$). **F.** Neighborhood scores of the representations, calculated using 11 neighbors (2-way ANOVA: model $F(3,32)=763.59$, $p<10^{-3}$, layer $F(1, 32)=3839.02$, $p<10^{-3}$, model x layer $F(3, 32)=66.50$, $p<10^{-3}$). **G.** Trustworthiness of the representations, calculated using 11 neighbors (2-way ANOVA: model $F(3,32)=498.69$, $p<10^{-3}$, layer $F(1, 32)=623.23$, $p<10^{-3}$, model x

layer $F(3, 32)=118.35, p<10^{-3}$). In all barplots the errorbars represent three standard deviations across $N=5$ initializations for each model. Stars denote significance with unpaired t-test (two-tailed) with Bonferroni's correction.

To complete our interpretability analysis, we visualized the hidden representations of all dANN and vANN models post-learning. The goal was to assess the amount of high-level information that is extracted by the first and second hidden layers across models (i.e., dendritic and somatic layers for dANNs, respectively). We applied the T-distributed stochastic neighbor embedding (TSNE), an algorithm that reduces the dimensionality and allows visualization of high-dimensional data⁷⁰. By visual inspection, we observed a change in the representation between the dendritic and somatic layers of dANN models, similarly to representations of vANN between its two hidden layers (**Figure 5A-D**). We quantified the separability of the representations using the silhouette and the neighborhood (NH) scores, which measure the global and local degree of separability, respectively (see *Methods*). In all dANN models, global and local separability was increased from the dendritic to the somatic layer (**Figure 5E-F**), something that we also observed in the hidden layers of the vANN. This means that the discriminatory power of both dANNs and vANN increases across layers in a similar way. This is in line with the findings of **Figure 4**, whereby the vANN is shown to have higher class-specificity than the dANNs in the first layer, and thus higher separability scores. Importantly, our results regarding the properties of the representations in low dimensional space reflect the properties of the high-dimensional data as shown by their high trustworthiness scores (**Figure 5G**). The latter measures the extent to which the local structure of the data is retained after projection to the lower-dimensional space. Values close

to 1 indicate high reliability. **Figure 5G** suggests that dANNs do a better job in retaining the structure of the original data in their representations -as measured by TSNE-, compared to vANNs. This is probably a result of the different strategy implemented by these networks.

Overall, our interpretability analysis reveals that dANNs use a different strategy than the vANN model to achieve accurate, robust, and efficient image classification: rather than becoming class-specific early on like the vANN, dANN models exhibit mixed-selectivity in both layers. This strategy is likely to underlie their ability to create more trustworthy representations of the input data, leading to high performance accuracy and reduced overfitting, while using significantly fewer and better utilized trainable parameters.

Dendritic benefits are more pronounced as the task difficulty increases

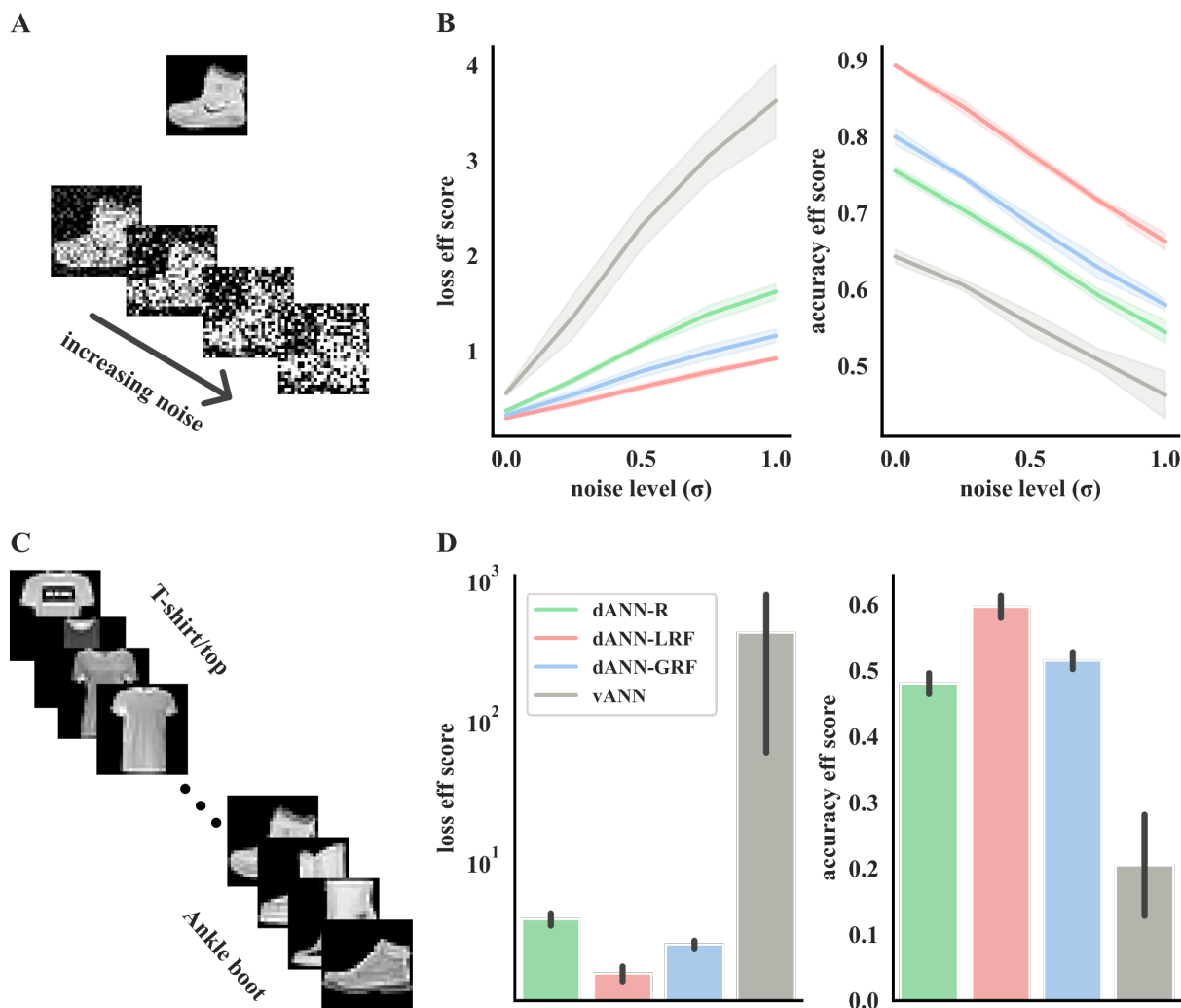


Figure 6. dANNs are more accurate and efficient than vANNs when inputs are noisy or presented in a sequential manner. **A.** An example of one FMNIST image with variable Gaussian noise. Sigma (σ) is the standard deviation of the Gaussian noise. **B.** Testing loss (*left*) and accuracy (*right*) efficiency scores for all models and noise levels. Shades represent three standard deviations across $N=5$ network initializations for each model. **C.** The sequential learning task. **D.** As in **B**, but showing the loss (*left*) and accuracy (*right*) efficiency scores for the sequential task. Errorbars denote three standard deviations across $N=5$ initializations for each model. See **Table 2** and **Supplementary Table 3** for the accuracy and loss values.

Our image discrimination results suggest that the difference between dANN and vANN models may be larger for more difficult tasks/datasets (see results for CIFAR10 in **Table 1**). To test this hypothesis, we constructed learning scenarios that are known to be challenging for ANN models.

First, we added Gaussian noise (with a variable σ and zero mean) to all images in the FMNIST dataset, thus creating new datasets of increasing classification difficulty (**Figure 6A**). We then selected the best vANN and the corresponding dANNs that matched its performance accuracy on FMNIST (from **Figure 2** and **Figure 3**) and tested their performance on the noisy datasets. We found that, while the performance of all models declined with increasing noise levels, dANNs demonstrated higher efficiency and resilience. This is evident by a slower increase rate for the loss and a slower drop rate for the accuracy efficiency scores, respectively, compared to vANNs (**Figure 6B**). In all cases, the best-performing dANN was the one with local RFs (dANN-LRF).

To confirm the advantage of dANN models on challenging tasks, we constructed a second learning scenario that remains challenging for traditional ANNs. In this task, models were fed with batches of inputs belonging to the same class in a sequential manner (**Figure 6C**). This process, which was repeated 50 times (epochs), results in models receiving information only from images of a single class during gradient calculation. As with the noisy task, dANN models were more accurate (**Table 2**), less variable across different initializations, and much more efficient than the vANN, as evidenced by their loss and accuracy efficiency scores (**Figure 6D**). The best-performing dANN was again the one with local RFs (dANN-LRF). Overall, these findings reinforce our claim that the addition of dendrites in ANNs enables

more accurate and robust learning, using orders of magnitude fewer parameters, and that these benefits are even more pronounced under challenging settings.

Table 2. Test accuracy obtained by each model on the sequential learning task, and their corresponding test loss, using the FMNIST dataset. Test accuracy and loss are listed as mean \pm standard deviation across $N=5$ initializations for each model.

MODEL PERFORMANCE – SEQUENTIAL LEARNING		
Models	Test accuracy (%)	Test loss
dANN	56.834 \pm 1.6748	339.4656 \pm 30.6265
dANN-LRF	59.658\pm1.5005	165.3191\pm17.8309
dANN-GRF	57.686 \pm 1.2854	237.5777 \pm 13.1761
vANN	28.458 \pm 9.4994	31346.5998 \pm 24085.2921

Discussion

Bio-inspired machine learning is one of the most dynamic branches of AI. Biological dendrites and their learning rules, are among the top candidates being explored, already showing highly promising results in artificial neural networks^{55,56,71,72}. Recent studies in dendritic networks focus on their potential to tackle difficult problems such as continual^{60,63} and multitask learning⁶⁵ and propose solutions to the credit assignment problem without backpropagation^{56,57}. However, the processing power and efficiency of biological networks, largely endowed by their dendrites, are still far from being matched by respective ANNs. Towards this goal, we focused on the structured connectivity and restricted sampling characteristics of dendrites, two prominent features that are conserved across brain regions

and species^{73,74}, suggesting that their role in information processing is likely to be very important.

We constructed a set of dendritic ANNs that leverage the structured connectivity and restricted sampling features of biological dendrites to enhance learning. dANNs are constructed as typical ANNs with two hidden layers, in which the first (dendritic) layer is connected in a sparse and structured manner to the second (somatic) layer so that it resembles the structured connectivity of biological dendrites to their respective somata. Input sampling was inspired by the receptive fields of neurons in the visual cortex^{67,74}, whereby dendrites (and neurons) sample only a restricted part of the visual space. We compared our models to vanilla ANNs across numerous image classification tasks and found that they are superior in performance accuracy, degree of overfitting, robustness to noise, and sequential learning. Compared to vANN, these benefits are achieved with orders of magnitude fewer trainable parameters, making dANNs more efficient and effective. As there is growing concern that the demand for computational resources to develop and maintain AI models and applications could lead to a significant increase in the electricity consumption of data centers worldwide⁷⁵, dANNs are especially valuable for edge computing and other energy-constrained scenarios. Even though we focused on simple ANNs that form the foundation of nearly all DL architectures, it is important to note that our study also offers a framework for integrating dendritic features into various models, such as convolutional neural networks, transformers, and others⁷⁶. This involves replacing the fully connected layers commonly found in deep learning architectures with our dANN model.

Other studies have also adopted dendritic properties in ANNs and DL models. These studies are different and complementary to ours in several ways. For example, one approach implemented dendrites as max-pooling or average-pooling layers^{63,64,77}, two methods that are extensively used in DL models⁷⁸. Other approaches were more abstract, modeling dendrites as a multiplicative component and/or using all-to-all connectivity from the input layer onto dendrites^{62,79-81}. Some methods use specific dendritic components, such as normalization of the weights or specific dendritic spikes, but their connectivity matrices become sparse using, for example, evolutionary algorithms, or they contain fully connected layers^{65,82,83}. Lastly, dendritic models incorporating local learning rules have been used to study how the brain solves the credit assignment problem, showing promising learning capabilities but are not easily applicable to large ML applications^{55,56,71}.

Inspired by⁵⁸, our modeling approach considers dendrites as an additional layer that provides weighted inputs to the somatic nodes. This means that dANN can be viewed as a sparse ANN from an ML perspective. In ANNs, sparsity can be achieved by pruning after training^{84,85}, using evolutionary algorithms^{86,87}, specific regularization^{88,89} during training, or iterative methods applied before training^{90,91}. Similar to the later approaches, in dANNs, the connectivity sparsity is handcrafted from the start, creating a fixed architecture that is significantly smaller than typical vANNs undergoing a pruning process. This makes training faster and more efficient, as no pruning is required. Furthermore, inputs to dendrites are not randomly allocated but can be constructed based on RFs, setting our model apart from traditional sparse networks that rely on random connectivity initialization. Finally, RFs are created before training and can be modified to capture the most essential characteristics of a

dataset. These attributes lend biological plausibility to our dANN models and are expected to be advantageous for neuromorphic hardware implementation, particularly when faced with space limitations and increased energy consumption resulting from lengthy node connections.

It is crucial to acknowledge the boundaries and limitations of our dANN architecture. In the implementation presented here, to maintain their initial connectivity, dANNs necessitate an extra boolean mask multiplication after every gradient descent step. This additional step results in a higher computational expense regarding floating-point operations. Moreover, during training, we employ the backpropagation algorithm and discard some gradients that aren't linked to an existing connection, potentially losing vital information from other gradient directions. Using locally computed gradients would overcome these limitations and further improve the efficiency/performance of our dANN models, but such an implementation is currently not possible with existing ML platforms and requires custom-made code. Finally, our dANN models consist of only two hidden layers, a dendritic and a somatic. Although deeper ANNs are likely to achieve better performance accuracy, our primary focus here is to show that even small dANNs can achieve efficient learning with few trainable parameters. Nevertheless, we believe our work is valuable as it offers new insights into the benefits, i.e., improved accuracy, less overfitting, and much fewer parameters, that can be gained by adopting dendritic features in ANNs of any size/depth.

Overall, we show that implementing dendritic properties can significantly enhance the learning capabilities of ANNs, making them both accurate and efficient. These findings hold

great promise as they suggest that integrating biological characteristics could be crucial for optimizing the sustainability and effectiveness of ML algorithms.

Methods

Network architectures

We have developed a range of traditional ANNs consisting of two hidden layers and an output layer that matches the number of classes. To create the dANN model, we first create two boolean masks that determine the synaptic weights between the input and dendritic layers, as well as the cable weights between dendritic and somatic layers. Once we have initialized the model, we apply these masks to achieve a sparse network with structured synaptic and cable weights (Eq. 1).

$$W_k \leftarrow W_k \odot M_k(1)$$

where W_k denotes the weights, M_k the boolean mask associated k -th layer, and \odot is the Hadamard (elementwise) product.

The calculation for the forward pass is obtained by linearly combining the inputs with the weights and adding the bias in each node of all layers. Finally, the output is obtained by passing the summation through a (nonlinear) activation function (Eq. 2).

$$A_k = f(W_k X_k + b_k)(2)$$

where X_k and A_k denote the inputs to the k -th layer and its activations, respectively. $f(\cdot)$ is the activation function.

In the output layer, we calculate the loss, which is then propagated back to calculate the gradients with respect to all trainable parameters respectively. To ensure the same connectivity as the original model, we zero out all gradients calculated in non-existent connections (Eq. 3).

$$\frac{\partial L}{\partial \vartheta} \leftarrow \frac{\partial L}{\partial \vartheta} \odot M_k(3)$$

where L is the loss and ϑ denotes the trainable parameters.

Synaptic connections

To define the input to the dendritic connectivity matrix, we utilize three distinct strategies. Our first approach involves random allocation, where each dendrite receives 16 inputs (pixels) which are randomly selected from the image (dANN-R). Our second approach utilizes local-constructed receptive fields (dANN-LRF), where each dendrite again receives 16 inputs (pixels), but this time they are sampled from a restricted part of the image. To do so, we randomly select a pixel to represent the center of the receptive field for each dendrite. In particular, the central pixel is drawn from a uniform distribution. Then, the 16 inputs are chosen from the 4x4 neighborhood of that pixel. The process is repeated for all dendrites. Finally, we utilize a global-constructed receptive field (dANN-GRF). In this approach, we select a pixel to represent the receptive field center for each soma instead of each dendrite. Then, the central pixel of each dendrite belonging to that soma has a central pixel drawn from a uniform distribution around the central somatic pixel. Finally, dendrites receive 16 inputs from the 4x4 neighborhood of their central pixel, as before.

Datasets

The dANN models are trained to classify images into one of their respective classes. The MNIST⁹² consists of handwritten digits from 0 to 9. Fashion MNIST⁹³ is an alternative to MNIST and consists of clothing images: T-shirt/top, trousers, pullover, dress, coat, sandal, shirt, sneaker, bag, and ankle boot. Kuzushiji MNIST⁹⁴ is a drop-in replacement for the MNIST dataset consisting of one Japanese character representing each of the ten rows of Hiragana. All of these datasets come with 60,000 training and 10,000 test images. Extended MNIST⁹⁵ follows the same conversion paradigm used to create the MNIST dataset. The result is a set of datasets that constitute more challenging classification tasks involving letters and digits. Here, we used the 47 balanced classes with 731,668 training and 82,587 testing images. All MNIST variants consist of 28x28 grayscale images. Finally, CIFAR-10⁹⁶ consists of images of objects or animals in ten classes: airplane, automobile, bird, cat, deer, dog, frog, horse, ship, and truck. The dataset contains 50,000 training and 10,000 test images. The images are 32x32 pixels in three color channels.

For our experiments, we trained the models with 90% of the training data, keeping the remaining 10% for validation. Once the training was complete, we evaluated the performance on the test set.

Hyperparameters

Our models were trained using the Adam optimization algorithm, with the default parameters of a learning rate of 0.001 and betas of 0.9 and 0.999. To ensure efficient training, we utilized a minibatch size of 128. The number of epochs was variable for each dataset but the same across models. Specifically, for MNIST, FMNIST, and KMNIST we

used 15, 20, and 20 epochs, respectively, whereas for EMNIST and CIFAR10 we used 50 epochs. For the sequential learning scenario, we used 50 epochs to train the models. In our dANN models, each dendrite receives inputs from 16 input neurons. We calculate the loss using the cross-entropy function and have set the activation function of all nodes to the Leaky Rectified Linear Unit (ReLU) with a negative slope of 0.1, except for the output nodes, which utilize the softmax activation function.

Efficiency scores

To calculate the efficiency scores for all networks, we formulated the accuracy (*aes*) and loss (*les*) efficiency scores, respectively. To do so, we normalized the accuracy and loss with a factor f that takes values from $[1, \infty]$ and is the ratio of the logarithm, with base 10, of the number of trainable parameters of a model i with the minimum number of trainable parameters of the compared models (Eq. 4).

$$f = \frac{\log_{10} k}{\min_m (\log_{10}(k_m))} \quad (4)$$

By dividing the accuracy by the factor f , the score remains in $[0, 100]$ while multiplying the loss with f the loss score remains in $[0, \infty]$ (Eq. 5).

$$aes = \frac{accuracy(\%)}{f}, les = loss \cdot f \quad (5)$$

where k_i denotes the number of trainable parameters of model i , and m denotes the compared models $m \in \{dANN - R, dANN - LRF, dANN - GRF, vANN\}$.

Using these scores, models with much more trainable parameters show lower accuracy efficiency scores and higher loss efficiency scores compared with models with less number of parameters.

Interpretability analysis

Synaptic, cable, and output weights: To display the learned weights, we constructed histograms with 20 bins and utilized kernel density estimation (KDE) to approximate the underlying distribution using a continuous probability density curve. The KDE plot smooths the observations with a Gaussian kernel, generating a continuous estimation. The histograms are built by concatenating the learned weights across $N=5$ initializations for each ANN model.

Entropy: To calculate the entropy for the first and second hidden layers, we used the activations of all nodes during evaluation against the test set. First, we created the hit matrix ($HM \in R^{n_{class} \times D}$) for each layer that assigns the number of times a node was activated (activity above zero) for images belonging to the same category.

To calculate normalized probabilities, we add an extra row to HM containing the number of times a node remained inactive. Thus, the summation across rows is equal to the number of data samples in the test set.

Obtaining the probability matrix by dividing the HM by the number of images, we calculate the entropy for each node in the k -th layer (Eq. 6).

$$H_k = - \sum_{i=1}^D p(x) \log_2 p(x) \quad (6)$$

We plot the entropy distributions using histograms with 20 bins and the KDE method to estimate a continuous probability density function. We removed inactive nodes from the analysis.

Selectivity: To calculate how selective a node is, we calculated how many categories it was activated for. We consider activity significant if a node was activated for over 400 images of a specific category. Thus, we ended with integers in $[1, n_{class}]$, with 1 denoting class-specificity and n_{class} total mixed-selectivity. As selectivity is a discrete metric, we plot the histograms with n_{class} bins and without using KDE.

Dimensionality reduction and analysis

To calculate the representations of the hidden layers, we used the t-distributed stochastic neighbor embedding (TSNE) dimensionality reduction method⁷⁰ with perplexity equal to 50. We chose this technique based on its widespread popularity and proven ability to preserve neighborhoods and clusters in projections. Activations for a given layer, the subject of our analysis, are extracted strictly for a random subset of 2,000 observations from the test sets to aid visual presentation. We visualize projections as scatterplots, with points colored to show their class. To assess the quality of the projection and its discriminatory power, we employ two metrics. The Silhouette score calculates the global structure of the projection. It shows if activations of images belonging to the same category are close in the reduced space⁹⁷, and the neighborhood hit score (NH) shows the local structure in the projection and indicates how well classes are visually separated^{98,99}.

Silhouette score is calculated using the mean intra-cluster distance (a) and the mean nearest-cluster distance (b) for each sample (Eq. 7).

$$s_i = \frac{b - a}{\max(a, b)}, i \in \{1, 2, \dots, n\} \quad (7)$$

and takes values in $[-1, 1]$, with values closer to 1 denoting good clustering and values close to 0 indicating overlapping clusters. Negative values indicate a sample has been assigned to the wrong cluster, as a different cluster is more similar. The Silhouette score is the average over all samples.

The NH denotes how similar a point is to its k nearest neighbors in the reduced space. For a given k , the NH for a point x is the percentage of the k -nearest neighbors that belong to the same class as x (Eq. 8).

$$NH(k) = \frac{1}{n} \sum_{i=1}^n \left\{ \frac{\sum_{j=1}^k l_j}{k} \right\}, l_j = 1 \text{ if } r_j \in C^{[x_i]} \text{ else } 0 \quad (8)$$

where $C^{[x_i]}$ denotes the category of the data point x_i , and r_j are the point in its neighborhood. Then the neighborhood hit score is calculated as an average across all points x in the dataset. The score is bounded in $[0, 1]$, with higher values denoting better neighborhood compactness and small values of misplaced data points. Here, we use $k=11$.

Trustworthiness is a metric that expresses the extent to which the local structure is retained after the dimensionality reduction¹⁰⁰ (Eq. 9).

$$T(k) = 1 - \frac{2}{nk(2n - 3k - 1)} \sum_{i=1}^n \sum_{j \in N_i^k} \max(0, (r(i, j) - k)) \quad (9)$$

where $r(i, j)$ denotes the rank of the datapoint j according to the pairwise distances between the low-dimensional datapoints, and N_i^k represents the k -nearest neighbors of datapoint i in the low-dimensional space, but not in the high-dimensional space. Thus, any unexpected nearest neighbors in the low-dimensional space are penalized proportionally to their rank in the high-dimensional space. The trustworthiness is within $[0, 1]$. Here, we use $k=11$.

Computing resources and software

All simulations were performed on a custom machine under the Debian GNU/Linux trixie/sid (kernel version 6.6.15-2) operating system with 64GB of RAM, Intel® Core™ i5-10400 CPU @ 2.90GHz, and an NVIDIA GeForce RTX 3080 Ti GPU @ 12GB. We implemented all models using the Keras 2.15.0 functional API¹⁰¹ with TensorFlow 2.15.0 backend¹⁰² under Python 3.9.18 (conda 23.7.4). For better handling of the training process, we used a custom training loop. For data analysis and visualization, we utilized various Python modules, including numpy 1.24.4¹⁰³, scikit-learn 1.4.1¹⁰⁴, pandas 1.5.3¹⁰⁵, matplotlib 3.8.3¹⁰⁶, seaborn 0.13.2¹⁰⁷ and seaborn-image 0.8.0¹⁰⁸.

Statistical Analysis

For all standard statistical tests (detailed in Figure legends), the significance level α was 0.05. To correct for multiple comparisons, α was divided by the number of tests according to the Bonferroni procedure. Throughout the Figures, p values are denoted by * ($p < 0.05$), ** ($p < 0.01$), and *** ($p < 0.001$). To compare the dependent value among different groups (models x layers), we used a two-way analysis of variance (ANOVA) followed by an unpaired t-test (two-tailed) with Bonferroni's correction whenever statistical difference was

observed for post hoc comparisons. The statistical analysis was performed using the pingouin 0.5.4 library¹⁰⁹.

References

1. Attwell, D. & Laughlin, S. B. An Energy Budget for Signaling in the Grey Matter of the Brain. *J. Cereb. Blood Flow Metab.* **21**, 1133–1145 (2001).
2. Luccioni, A. S., Jernite, Y. & Strubell, E. Power Hungry Processing: Watts Driving the Cost of AI Deployment? Preprint at <http://arxiv.org/abs/2311.16863> (2023).
3. Strubell, E., Ganesh, A. & McCallum, A. Energy and Policy Considerations for Deep Learning in NLP. in *Proceedings of the 57th Annual Meeting of the Association for Computational Linguistics* (eds. Korhonen, A., Traum, D. & Màrquez, L.) 3645–3650 (Association for Computational Linguistics, Florence, Italy, 2019).
4. Mehonic, A. & Kenyon, A. J. Brain-inspired computing needs a master plan. *Nature* **604**, 255–260 (2022).
5. McCloskey, M. & Cohen, N. J. Catastrophic Interference in Connectionist Networks: The Sequential Learning Problem. in *Psychology of Learning and Motivation* vol. 24 109–165 (Elsevier, 1989).
6. Abraham, W. C. & Robins, A. Memory retention – the synaptic stability versus plasticity dilemma. *Trends Neurosci.* **28**, 73–78 (2005).
7. Mesnil, G. *et al.* Unsupervised and Transfer Learning Challenge: a Deep Learning Approach. in *Proceedings of ICML Workshop on Unsupervised and Transfer Learning* 97–110 (JMLR Workshop and Conference Proceedings, 2012).
8. LeCun, Y., Bengio, Y. & Hinton, G. Deep learning. *Nature* **521**, 436–444 (2015).

9. Guo, Y. *et al.* Deep learning for visual understanding: A review. *Neurocomputing* **187**, 27–48 (2016).
10. Chai, J. & Li, A. Deep Learning in Natural Language Processing: A State-of-the-Art Survey. in *2019 International Conference on Machine Learning and Cybernetics (ICMLC)* 1–6 (IEEE, Kobe, Japan, 2019).
11. Silver, D. *et al.* Mastering the game of Go with deep neural networks and tree search. *Nature* **529**, 484–489 (2016).
12. Fuchs, F., Song, Y., Kaufmann, E., Scaramuzza, D. & Durr, P. Super-Human Performance in Gran Turismo Sport Using Deep Reinforcement Learning. *IEEE Robot. Autom. Lett.* **6**, 4257–4264 (2021).
13. Ying, X. An Overview of Overfitting and its Solutions. *J. Phys. Conf. Ser.* **1168**, 022022 (2019).
14. Yang, T.-J., Chen, Y.-H., Emer, J. & Sze, V. A method to estimate the energy consumption of deep neural networks. in *2017 51st Asilomar Conference on Signals, Systems, and Computers* 1916–1920 (IEEE, Pacific Grove, CA, USA, 2017).
15. Nazaré, T. S., Da Costa, G. B. P., Contato, W. A. & Ponti, M. Deep Convolutional Neural Networks and Noisy Images. in *Progress in Pattern Recognition, Image Analysis, Computer Vision, and Applications* (eds. Mendoza, M. & Velastín, S.) vol. 10657 416–424 (Springer International Publishing, Cham, 2018).
16. Dodge, S. & Karam, L. Understanding how image quality affects deep neural networks. in *2016 Eighth International Conference on Quality of Multimedia Experience (QoMEX)* 1–6 (IEEE, Lisbon, Portugal, 2016).

17. Parisi, G. I., Kemker, R., Part, J. L., Kanan, C. & Wermter, S. Continual lifelong learning with neural networks: A review. *Neural Netw.* **113**, 54–71 (2019).
18. McCulloch, W. S. & Pitts, W. A logical calculus of the ideas immanent in nervous activity. *Bull. Math. Biophys.* **5**, 115–133 (1943).
19. Rumelhart, D. E., Hinton, G. E. & Williams, R. J. Learning representations by back-propagating errors. *Nature* **323**, 533–536 (1986).
20. Spruston, N. Pyramidal neurons: dendritic structure and synaptic integration. *Nat. Rev. Neurosci.* **9**, 206–221 (2008).
21. Major, G., Larkum, M. E. & Schiller, J. Active Properties of Neocortical Pyramidal Neuron Dendrites. *Annu. Rev. Neurosci.* **36**, 1–24 (2013).
22. Larkum, M. E., Wu, J., Duverdin, S. A. & Gidon, A. The Guide to Dendritic Spikes of the Mammalian Cortex In Vitro and In Vivo. *Neuroscience* **489**, 15–33 (2022).
23. Poirazi, P., Brannon, T. & Mel, B. W. Pyramidal Neuron as Two-Layer Neural Network. *Neuron* **37**, 989–999 (2003).
24. Tzivilivaki, A., Kastellakis, G. & Poirazi, P. Challenging the point neuron dogma: FS basket cells as 2-stage nonlinear integrators. *Nat. Commun.* **10**, 3664 (2019).
25. Beniaguev, D., Segev, I. & London, M. Single cortical neurons as deep artificial neural networks. *Neuron* **109**, 2727–2739.e3 (2021).
26. Häusser, M. & Mel, B. Dendrites: bug or feature? *Curr. Opin. Neurobiol.* **13**, 372–383 (2003).
27. Poirazi, P. & Papoutsis, A. Illuminating dendritic function with computational models. *Nat. Rev. Neurosci.* **21**, 303–321 (2020).

28. Larkum, M. A cellular mechanism for cortical associations: an organizing principle for the cerebral cortex. *Trends Neurosci.* **36**, 141–151 (2013).
29. Gidon, A. *et al.* Dendritic action potentials and computation in human layer 2/3 cortical neurons. *Science* **367**, 83–87 (2020).
30. Shepherd, G. M. & Brayton, R. K. Logic operations are properties of computer-simulated interactions between excitable dendritic spines. *Neuroscience* **21**, 151–165 (1987).
31. Harnett, M. T., Makara, J. K., Spruston, N., Kath, W. L. & Magee, J. C. Synaptic amplification by dendritic spines enhances input cooperativity. *Nature* **491**, 599–602 (2012).
32. Schachter, M. J., Oesch, N., Smith, R. G. & Taylor, W. R. Dendritic Spikes Amplify the Synaptic Signal to Enhance Detection of Motion in a Simulation of the Direction-Selective Ganglion Cell. *PLoS Comput. Biol.* **6**, e1000899 (2010).
33. Ariav, G., Polsky, A. & Schiller, J. Submillisecond Precision of the Input-Output Transformation Function Mediated by Fast Sodium Dendritic Spikes in Basal Dendrites of CA1 Pyramidal Neurons. *J. Neurosci.* **23**, 7750–7758 (2003).
34. Softky, W. Sub-millisecond coincidence detection in active dendritic trees. *Neuroscience* **58**, 13–41 (1994).
35. Roome, C. J. & Kuhn, B. Dendritic coincidence detection in Purkinje neurons of awake mice. *eLife* **9**, e59619 (2020).
36. Stuart, G. J. & Häusser, M. Dendritic coincidence detection of EPSPs and action potentials. *Nat. Neurosci.* **4**, 63–71 (2001).

37. Naud, R. & Sprekeler, H. Sparse bursts optimize information transmission in a multiplexed neural code. *Proc. Natl. Acad. Sci.* **115**, (2018).
38. Anandan, E. S., Husain, R. & Seluakumaran, K. Auditory attentional filter in the absence of masking noise. *Atten. Percept. Psychophys.* **83**, 1737–1751 (2021).
39. Benezra, S. E., Patel, K. B., Campos, C. P., Hillman, E. M. C. & Bruno, R. M. *Learning Enhances Behaviorally Relevant Representations in Apical Dendrites*. Preprint at <https://www.biorxiv.org/content/10.1101/2021.11.10.468144v2> (2024).
40. Takahashi, N., Oertner, T. G., Hegemann, P. & Larkum, M. E. Active cortical dendrites modulate perception. *Science* **354**, 1587–1590 (2016).
41. Takahashi, N. *et al.* Active dendritic currents gate descending cortical outputs in perception. *Nat. Neurosci.* **23**, 1277–1285 (2020).
42. Xu, T. *et al.* Rapid formation and selective stabilization of synapses for enduring motor memories. *Nature* **462**, 915–919 (2009).
43. Otor, Y. *et al.* Dynamic compartmental computations in tuft dendrites of layer 5 neurons during motor behavior. *Science* **376**, 267–275 (2022).
44. Lai, C. S. W., Adler, A. & Gan, W.-B. Fear extinction reverses dendritic spine formation induced by fear conditioning in the mouse auditory cortex. *Proc. Natl. Acad. Sci.* **115**, 9306–9311 (2018).
45. Xu, Z. *et al.* Fear conditioning and extinction induce opposing changes in dendritic spine remodeling and somatic activity of layer 5 pyramidal neurons in the mouse motor cortex. *Sci. Rep.* **9**, 4619 (2019).

46. Letzkus, J. J. *et al.* A disinhibitory microcircuit for associative fear learning in the auditory cortex. *Nature* **480**, 331–335 (2011).
47. Kastellakis, G., Silva, A. J. & Poirazi, P. Linking Memories across Time via Neuronal and Dendritic Overlaps in Model Neurons with Active Dendrites. *Cell Rep.* **17**, 1491–1504 (2016).
48. Malakasis, N., Chavlis, S. & Poirazi, P. *Synaptic Turnover Promotes Efficient Learning in Bio-Realistic Spiking Neural Networks.* Preprint at <http://biorxiv.org/content/10.1101/2023.05.22.541722> (2023).
49. Poirazi, P. & Mel, B. W. Impact of Active Dendrites and Structural Plasticity on the Memory Capacity of Neural Tissue. *Neuron* **29**, 779–796 (2001).
50. Kaifosh, P. & Losonczy, A. Mnemonic Functions for Nonlinear Dendritic Integration in Hippocampal Pyramidal Circuits. *Neuron* **90**, 622–634 (2016).
51. Makarov, R., Pagkalos, M. & Poirazi, P. Dendrites and efficiency: Optimizing performance and resource utilization. *Curr. Opin. Neurobiol.* **83**, 102812 (2023).
52. Pagkalos, M., Makarov, R. & Poirazi, P. Leveraging dendritic properties to advance machine learning and neuro-inspired computing. *Curr. Opin. Neurobiol.* **85**, 102853 (2024).
53. Chavlis, S. & Poirazi, P. Drawing inspiration from biological dendrites to empower artificial neural networks. *Curr. Opin. Neurobiol.* **70**, 1–10 (2021).
54. Acharya, J. *et al.* Dendritic Computing: Branching Deeper into Machine Learning. *Neuroscience* **489**, 275–289 (2022).

55. Guerguiev, J., Lillicrap, T. P. & Richards, B. A. Towards deep learning with segregated dendrites. *eLife* **6**, e22901 (2017).
56. Payeur, A., Guerguiev, J., Zenke, F., Richards, B. A. & Naud, R. Burst-dependent synaptic plasticity can coordinate learning in hierarchical circuits. *Nat. Neurosci.* **24**, 1010–1019 (2021).
57. Illing, B., Ventura, J., Bellec, G. & Gerstner, W. Local plasticity rules can learn deep representations using self-supervised contrastive predictions. in *Advances in Neural Information Processing Systems* (eds. Ranzato, M., Beygelzimer, A., Dauphin, Y., Liang, P. S. & Vaughan, J. W.) vol. 34 30365–30379 (Curran Associates, Inc., 2021).
58. Jones, I. S. & Kording, K. P. Might a Single Neuron Solve Interesting Machine Learning Problems Through Successive Computations on Its Dendritic Tree? *Neural Comput.* **33**, 1554–1571 (2021).
59. Körding, K. P. & König, P. Supervised and unsupervised learning with two sites of synaptic integration. *J. Comput. Neurosci.* **11**, 207–215 (2001).
60. Kirkpatrick, J. *et al.* Overcoming catastrophic forgetting in neural networks. *Proc. Natl. Acad. Sci.* **114**, 3521–3526 (2017).
61. Siegel, M., Körding, K. P. & König, P. [No title found]. *J. Comput. Neurosci.* **8**, 161–173 (2000).
62. Tang, C. *et al.* Dendritic Neural Network: A Novel Extension of Dendritic Neuron Model. *IEEE Trans. Emerg. Top. Comput. Intell.* 1–12 (2024).
63. Iyer, A. *et al.* Avoiding Catastrophe: Active Dendrites Enable Multi-Task Learning in Dynamic Environments. *Front. Neurobotics* **16**, 846219 (2022).

64. Wu, X., Liu, X., Li, W. & Wu, Q. Improved Expressivity Through Dendritic Neural Networks. in *Advances in Neural Information Processing Systems* (eds. Bengio, S. et al.) vol. 31 (Curran Associates, Inc., 2018).
65. Wybo, W. A. M. *et al.* NMDA-driven dendritic modulation enables multitask representation learning in hierarchical sensory processing pathways. *Proc. Natl. Acad. Sci.* **120**, e2300558120 (2023).
66. Ringach, D. L. Mapping receptive fields in primary visual cortex. *J. Physiol.* **558**, 717–728 (2004).
67. Bair, W. Visual receptive field organization. *Curr. Opin. Neurobiol.* **15**, 459–464 (2005).
68. Ascoli, G. A., Donohue, D. E. & Halavi, M. NeuroMorpho.Org: A Central Resource for Neuronal Morphologies. *J. Neurosci.* **27**, 9247–9251 (2007).
69. Nusrat, I. & Jang, S.-B. A Comparison of Regularization Techniques in Deep Neural Networks. *Symmetry* **10**, 648 (2018).
70. Maaten, L. van der & Hinton, G. Visualizing Data using t-SNE. *J. Mach. Learn. Res.* **9**, 2579–2605 (2008).
71. Sacramento, J., Ponte Costa, R., Bengio, Y. & Senn, W. Dendritic cortical microcircuits approximate the backpropagation algorithm. in *Advances in Neural Information Processing Systems* (eds. Bengio, S. et al.) vol. 31 (Curran Associates, Inc., 2018).
72. Sacramento, J., Costa, R. P., Bengio, Y. & Senn, W. Dendritic error backpropagation in deep cortical microcircuits. Preprint at <http://arxiv.org/abs/1801.00062> (2017).

73. Holley, Z. L., Bland, K. M., Casey, Z. O., Handwerk, C. J. & Vidal, G. S. Cross-Regional Gradient of Dendritic Morphology in Isochronically-Sourced Mouse Supragranular Pyramidal Neurons. *Front. Neuroanat.* **12**, 103 (2018).
74. Gaucher, Q. *et al.* Complexity of frequency receptive fields predicts tonotopic variability across species. *eLife* **9**, e53462 (2020).
75. De Vries, A. The growing energy footprint of artificial intelligence. *Joule* **7**, 2191–2194 (2023).
76. Sarker, I. H. Deep Learning: A Comprehensive Overview on Techniques, Taxonomy, Applications and Research Directions. *SN Comput. Sci.* **2**, 420 (2021).
77. Wu, X. *et al.* Mitigating Communication Costs in Neural Networks: The Role of Dendritic Nonlinearity. Preprint at <http://arxiv.org/abs/2306.11950> (2023).
78. Zhao, L. & Zhang, Z. A improved pooling method for convolutional neural networks. *Sci. Rep.* **14**, 1589 (2024).
79. Ji, J., Gao, S., Cheng, J., Tang, Z. & Todo, Y. An approximate logic neuron model with a dendritic structure. *Neurocomputing* **173**, 1775–1783 (2016).
80. Todo, Y., Tamura, H., Yamashita, K. & Tang, Z. Unsupervised learnable neuron model with nonlinear interaction on dendrites. *Neural Netw.* **60**, 96–103 (2014).
81. Zhang, Y. *et al.* A Lightweight Multi-Dendritic Pyramidal Neuron Model with Neural Plasticity on Image Recognition. *IEEE Trans. Artif. Intell.* 1–13 (2024).
82. Bird, A. D., Jedlicka, P. & Cuntz, H. Dendritic normalisation improves learning in sparsely connected artificial neural networks. *PLOS Comput. Biol.* **17**, e1009202 (2021).

83. Hodassman, S., Vardi, R., Tugendhaft, Y., Goldental, A. & Kanter, I. Efficient dendritic learning as an alternative to synaptic plasticity hypothesis. *Sci. Rep.* **12**, 6571 (2022).
84. Mengiste, S. A., Aertsen, A. & Kumar, A. Effect of edge pruning on structural controllability and observability of complex networks. *Sci. Rep.* **5**, 18145 (2015).
85. Han, S., Pool, J., Tran, J. & Dally, W. Learning both Weights and Connections for Efficient Neural Network. in *Advances in Neural Information Processing Systems* (eds. Cortes, C., Lawrence, N., Lee, D., Sugiyama, M. & Garnett, R.) vol. 28 (Curran Associates, Inc., 2015).
86. Liu, Z. *et al.* Learning Efficient Convolutional Networks through Network Slimming. in *2017 IEEE International Conference on Computer Vision (ICCV)* 2755–2763 (IEEE, Venice, 2017).
87. Mocanu, D. C. *et al.* Scalable training of artificial neural networks with adaptive sparse connectivity inspired by network science. *Nat. Commun.* **9**, 2383 (2018).
88. Louizos, C., Welling, M. & Kingma, D. P. Learning Sparse Neural Networks through L₀ Regularization. in (2018).
89. Scardapane, S., Comminiello, D., Hussain, A. & Uncini, A. Group sparse regularization for deep neural networks. *Neurocomputing* **241**, 81–89 (2017).
90. Patil, S. M. & Dvornik, C. PHEW: Constructing Sparse Networks that Learn Fast and Generalize Well without Training Data. in *Proceedings of the 38th International Conference on Machine Learning* 8432–8442 (PMLR, 2021).

91. Tanaka, H., Kunin, D., Yamins, D. L. & Ganguli, S. Pruning neural networks without any data by iteratively conserving synaptic flow. in *Advances in Neural Information Processing Systems* vol. 33 6377–6389 (Curran Associates, Inc., 2020).
92. Lecun, Y., Bottou, L., Bengio, Y. & Haffner, P. Gradient-based learning applied to document recognition. *Proc. IEEE* **86**, 2278–2324 (1998).
93. Xiao, H., Rasul, K. & Vollgraf, R. Fashion-MNIST: a Novel Image Dataset for Benchmarking Machine Learning Algorithms. Preprint at <http://arxiv.org/abs/1708.07747> (2017).
94. Clanuwat, T. *et al.* Deep Learning for Classical Japanese Literature. Preprint at <http://arxiv.org/abs/1812.01718> (2018).
95. Cohen, G., Afshar, S., Tapson, J. & van Schaik, A. EMNIST: an extension of MNIST to handwritten letters. Preprint at <http://arxiv.org/abs/1702.05373> (2017).
96. Krizhevsky, A. Learning Multiple Layers of Features from Tiny Images. (2009).
97. Rousseeuw, P. J. Silhouettes: A graphical aid to the interpretation and validation of cluster analysis. *J. Comput. Appl. Math.* **20**, 53–65 (1987).
98. Paulovich, F. V., Nonato, L. G., Minghim, R. & Levkowitz, H. Least Square Projection: A Fast High-Precision Multidimensional Projection Technique and Its Application to Document Mapping. *IEEE Trans. Vis. Comput. Graph.* **14**, 564–575 (2008).
99. Rauber, P. E., Fadel, S. G., Falcao, A. X. & Telea, A. C. Visualizing the Hidden Activity of Artificial Neural Networks. *IEEE Trans. Vis. Comput. Graph.* **23**, 101–110 (2017).

100. Maaten, L. van der. Learning a Parametric Embedding by Preserving Local Structure. in *Proceedings of the Twelfth International Conference on Artificial Intelligence and Statistics* 384–391 (PMLR, 2009).
101. Chollet, F. & and others. Keras. (2015).
102. Martín Abadi, Ashish Agarwal, Paul Barham, Eugene Brevdo, *et al.* TensorFlow: Large-scale machine learning on heterogeneous systems.
103. Harris, C. R. *et al.* Array programming with NumPy. *Nature* **585**, 357–362 (2020).
104. Pedregosa, F. *et al.* Scikit-learn: Machine Learning in Python. *J. Mach. Learn. Res.* **12**, 2825–2830 (2011).
105. McKinney, W. pandas: a Foundational Python Library for Data Analysis and Statistics. in (2011).
106. Hunter, J. D. Matplotlib: A 2D Graphics Environment. *Comput. Sci. Eng.* **9**, 90–95 (2007).
107. Waskom, M. L. seaborn: statistical data visualization. *J. Open Source Softw.* **6**, 3021 (2021).
108. seaborn-image: image data visualization.
109. Vallat, R. Pingouin: statistics in Python. *J. Open Source Softw.* **3**, 1026 (2018).

Acknowledgments

The authors would like to thank Michalis Pagkalos, Dr. Athanasia Papoutsis, Prof. Blake Richards, Ioannis-Rafail Tzonevrakis, Dr. Eirini Troulinou, and Prof. Grigorios Tsagkatakis for their valuable and constructive feedback. This work was supported by NIH

(1R01MH124867-02) to P.P., the European Commission (H2020-FETOPEN-2018-2019-2020-01, FET-Open Challenging Current Thinking, NEUREKA GA-863245) to P.P.

Author contributions

S.C. and P.P. conceived the project, designed the experiments, and wrote the manuscript.

S.C. implemented the models, performed the experiments, analyzed the data, and created the Figures. P.P. supervised and funded the project.

Competing interests

The authors declare no competing interests.

Data availability

The source code that generates all Figures and the data that support this study are accessible on GitHub. We will release the repository link upon publication.

Computer code

The code underlying this study will be available on GitHub and accessed on Zenodo.

Supplementary Material

Supplementary Table 1. Minimum test loss scores obtained by each model on five benchmark datasets across various configurations and their corresponding test accuracy. Performance accuracy is listed as mean \pm standard deviation across $N=5$ initializations for each model.

	MODEL PERFORMANCE – MINIMUM LOSS				
Models	MNIST	FMNIST	KMINST	EMNIST	CIFAR10
	Test loss				
dANN-R	0.0644 \pm 0.0013	0.3152 \pm 0.0093	0.4880 \pm 0.0044	0.6282 \pm 0.0068	1.3771 \pm 0.0067
dANN-LRF	0.0483 \pm 0.0018	0.2871\pm0.0021	0.4342\pm0.0054	0.5675 \pm 0.0070	1.2528\pm0.0141
dANN-GRF	0.0471\pm0.0022	0.2879 \pm 0.0040	0.4615 \pm 0.0133	0.5317\pm0.0034	1.2732 \pm 0.0065
vANN	0.0864 \pm 0.0089	0.3579 \pm 0.0072	0.6905 \pm 0.0255	0.6861 \pm 0.0101	1.5297 \pm 0.0256
	Test accuracy (%)				
dANN-R	98.090 \pm 0.0583	89.108 \pm 0.1955	87.260 \pm 0.1346	80.986 \pm 0.2621	52.044 \pm 0.0172
dANN-LRF	98.466 \pm 0.1058	90.194\pm0.0543	89.070 \pm 0.1144	82.638 \pm 0.2798	56.076\pm0.3200
dANN-GRF	98.576\pm0.0809	89.996 \pm 0.2132	88.460 \pm 0.1872	83.520\pm0.1262	55.478 \pm 0.2848
vANN	97.858 \pm 0.2811	88.122 \pm 0.1492	91.194\pm0.3330	80.219 \pm 0.2291	46.680 \pm 0.8106

Supplementary Table 2. Characterization of probability density functions is shown in **Figure 4A**.

Skewness, kurtosis, and range are calculated.

models	First hidden layer			Second hidden layer			Output layer		
	kurtosis	skewness	range	kurtosis	skewness	range	kurtosis	skewness	range
dANN-R	2.741	-0.308	2.961	0.088	-0.124	3.261	0.857	-0.753	3.092
dANN-LRF	2.157	-0.372	4.082	-0.103	0.074	4.540	1.192	-0.510	3.496
dANN-GRF	3.457	-0.545	4.700	0.638	0.001	4.173	1.393	-0.561	2.869
vANN	2.814	-0.234	2.019	2.059	0.090	1.373	1.905	-0.796	0.805

Supplementary Table 3. Test accuracy obtained by each model on five noise levels, i.e., increasing the standard deviation of the Gaussian noise, and their corresponding test loss against the FMNIST noisy dataset. Test accuracy and loss are listed as mean \pm standard deviation across $N=5$ initializations for each model.

MODEL PERFORMANCE – NOISY IMAGES					
Models	$\sigma=0.0$	$\sigma=0.25$	$\sigma=0.5$	$\sigma=0.75$	$\sigma=1.0$
Test accuracy (%)					
dANN-R	89.392 \pm 0.2071	83.388 \pm 0.2340	77.108 \pm 0.2064	70.206 \pm 0.3007	64.456 \pm 0.5200
dANN-LRF	89.310 \pm 0.0514	83.926 \pm 0.2560	77.744\pm0.1853	71.73\pm0.1393	66.288\pm0.3290
dANN-GRF	89.616\pm0.3628	83.718 \pm 0.1289	76.864 \pm 0.3725	70.490 \pm 0.4438	64.996 \pm 0.2247
vANN	89.288 \pm 0.3654	84.178\pm0.2922	77.054 \pm 0.6884	70.624 \pm 0.5920	64.186 \pm 1.2748
Test loss					
dANN-R	0.3167 \pm 0.0035	0.5896 \pm 0.0078	0.8985 \pm 0.0072	1.176 \pm 0.0221	1.3742 \pm 0.0206
dANN-LRF	0.2997 \pm 0.0018	0.4519\pm0.0081	0.6224\pm0.0079	0.7826\pm0.0098	0.9251\pm0.0045
dANN-GRF	0.2932\pm0.0086	0.4868 \pm 0.0113	0.7033 \pm 0.0159	0.8827 \pm 0.0202	1.0381 \pm 0.0185
vANN	0.404 \pm 0.0066	0.9869 \pm 0.0492	1.6652 \pm 0.0528	2.196 \pm 0.0583	2.6139 \pm 0.0827

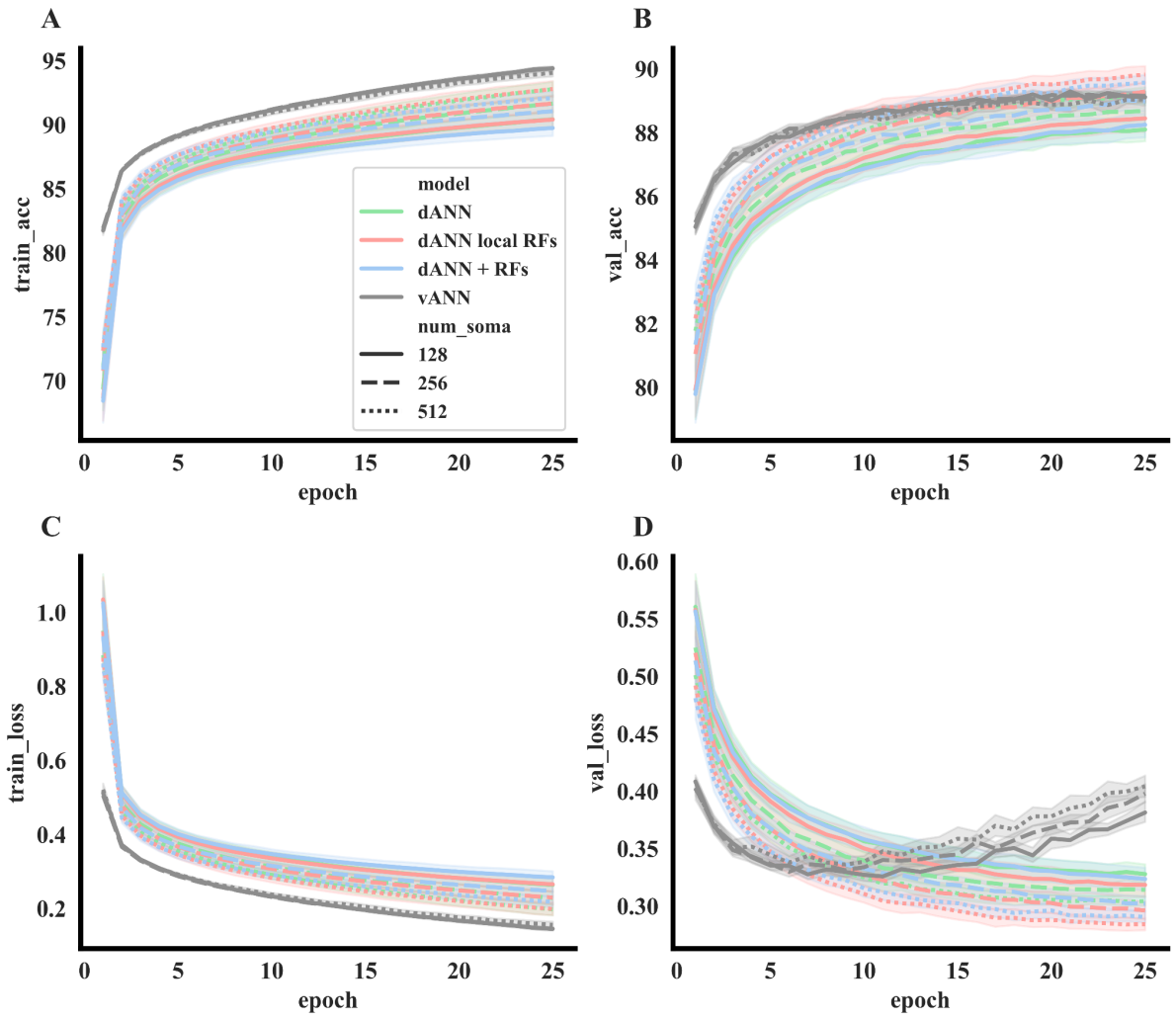


Figure S1. Training and validation process of all models. **A.** Training accuracy. **B.** Validation accuracy. **C.** Train loss. **D.** Validation loss. Shades denote standard deviation calculated across $N=5$ initializations for each model.

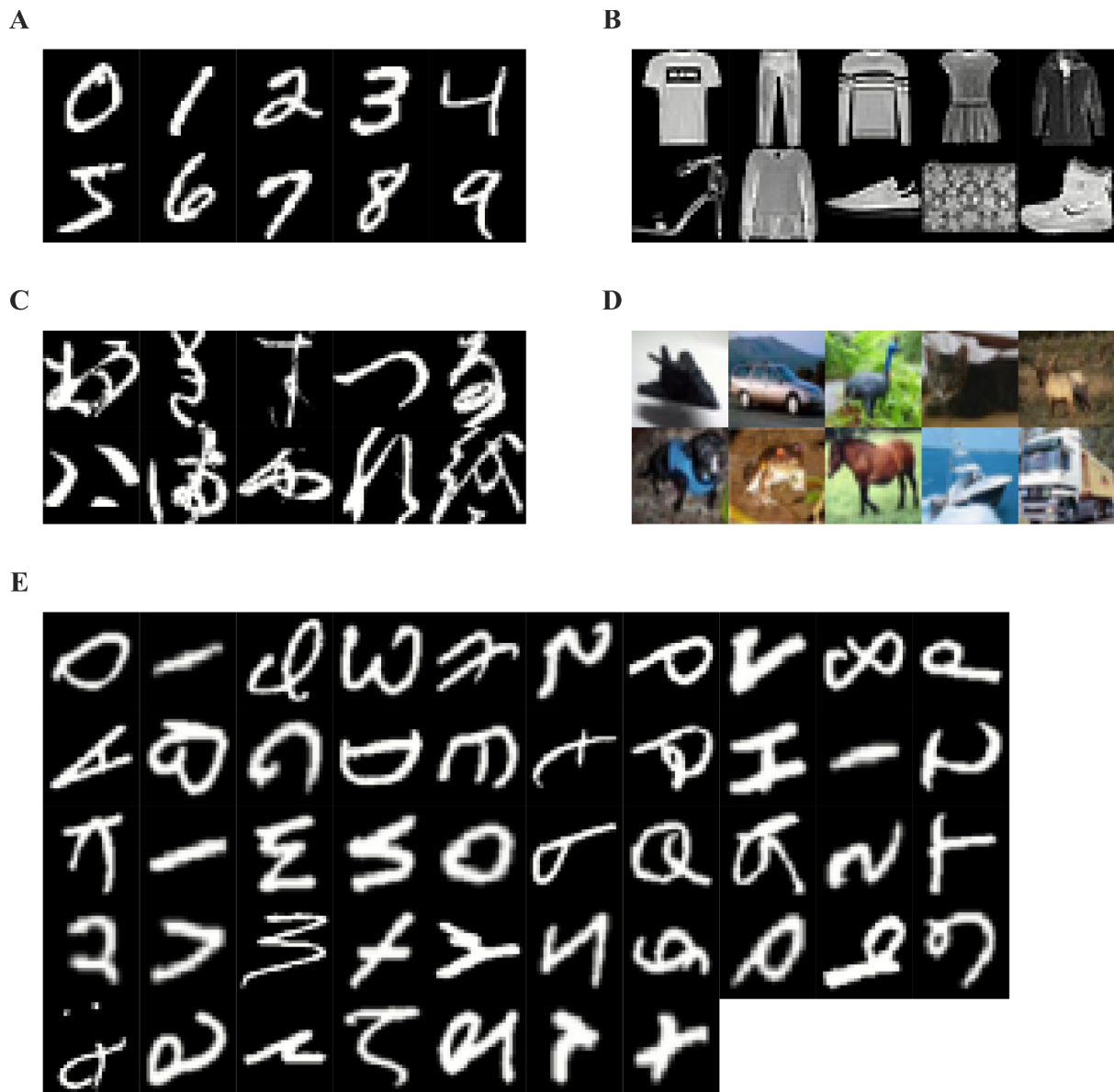


Figure S2. The classification benchmark datasets. **A.** The MNIST dataset. **B.** The Fashion MNIST (FMNSIT) dataset. **C.** The Kuzushiji MNIST (KMNIST) dataset. **D.** The CIFAR10 dataset. **E.** The Extended MNIST (EMNIST) dataset.